Research Square

Preprints are preliminary reports that have not undergone peer review.
They should not be considered conclusive, used to inform clinical practice,
or referenced by the media as validated information.

Rigid-flexible coupling dynamics for bionic body-caudal-fin propulsion based on Timoshenko beam theory

Zhenwei Sun
Xi'an University of Architecture and Technology
Xinrui Li
Xi'an University of Architecture and Technology
Yixiang Sui
Northwestern Polytechnical University
Yanbiao Zhao
Northwestern Polytechnical University
Dongbo Li
Xi'an University of Architecture and Technology
Yilin Qu
quyilin_95@126.com

Northwestern Polytechnical University

Research Article

Keywords: Rigid-flexible coupling dynamics, Timoshenko beam theory, Morison equation, Floating reference frame, propulsion performance

Posted Date: October 7th, 2026

DOI: https://doi.org/10.21203/rs.3.rs-11003475/v1

License: This work is licensed under a Creative Commons Attribution 4.0 International License.
Read Full License

Additional Declarations: No competing interests reported.

Rigid-flexible coupling dynamics for bionic body-caudal-fin propulsion based on Timoshenko beam theory

Zhenwei Sun[1], Xinrui Li[1], Yixiang Sui[2], Yanbiao Zhao[2], Dongbo Li[1], Yilin Qu[2,3,*]

1. Department of Structural Engineering, School of Civil Engineering, Xi'an University of Architecture and Technology, Xi'an, 710055, China

2. School of Marine Science and Technology, Northwestern Polytechnical University, Xi'an, Shaanxi 710072, China

3. Unmanned Vehicle Innovation Center, Ningbo Institute of NPU, Ningbo, Zhejiang 315048, China

*Corresponding author: quyilin_95@126.com (Y.Q.)

Abstract

Accurately predicting the rigid-flexible coupled dynamics of biomimetic body-caudal-fin (BCF) propulsors under transient hydrodynamic loads is crucial for underwater vehicle design. Classical Euler-Bernoulli theory, by neglecting transverse shear and rotary inertia, exhibits limitations under low-slenderness or high-frequency conditions. Therefore, this paper establishes a nonlinear rigid-flexible dynamic model using Timoshenko beam theory. By integrating the generalized principle of virtual work with the Morison equation, an analytical expression for transient thrust featuring a spatial slope correction is deduced, enabling accurate projection of local fluid forces onto the global coordinate system. The model is quantitatively validated through underwater oscillation experiments. Analyses reveal that flexible deformation breaks hydrodynamic symmetry, acting as the fundamental mechanism for thrust generation. Quantitatively, a 2-mm moderately flexible beam achieves a 100-mm tip deflection, producing significant asymmetric net thrust, whereas a stiffer counterpart yields an 80-mm deflection with markedly weakened thrust. Geometrically, propulsion approaches zero for excessively thick (5-mm) beams but increases linearly with beam width. Under high-frequency, small-amplitude conditions (e.g., 0.8 Hz, $\pi/6$ amplitude), the transient thrust waveform exhibits distinct nonlinear distortion and asymmetry. This originates from the dramatic amplification of transverse shear and rotary inertia effects unique to

Timoshenko beams. Ultimately, this theoretical framework overcomes the limitations of classical assumptions, providing a solid foundation for the parametric design of flexible propulsors.

Keywords**:** Rigid-flexible coupling dynamics; Timoshenko beam theory; Morison equation; Floating reference frame; propulsion performance

1. Introduction

Underwater biomimetic robots based on body-caudal fin (BCF) propulsion have become a research focus in marine engineering owing to their high efficiency and maneuverability [1-6]. In such systems, a rigid mechanism (e.g., a servo hub) drives a flexible caudal fin to perform large-amplitude periodic oscillations in the flow field, which is the primary means of generating effective net thrust [7-9]. During swimming, the flexible appendage experiences a large-scale macroscopic rigid-body motion driven by the actuating mechanism, while simultaneously undergoing local elastic bending deformation induced by the combined action of periodic hydrodynamic loads and internal inertial forces. This transient deformation, in turn, reconfigures the instantaneous shape and angle of attack of the fin, thereby dynamically modulating the direction and magnitude of the net thrust [10-12]. This process is essentially a rigid-flexible coupling dynamic problem, characterized by the strong nonlinear interaction between the overall rigid-body continuous motion and the local elastic deformation within the structure itself, which is further complicated by alternating fluid forces [13]. Experimental observations have shown that caudal fins of different stiffnesses exhibit distinct propulsion characteristics [14]; appropriate structural flexibility can enhance propulsive performance [15, 16], and a proper stiffness match can significantly improve swimming efficiency [17, 18]. To achieve systematic optimization of propulsion efficiency at the physical parameter level, it is crucial to establish an accurate theoretical analytical model that can reveal the intrinsic mapping relationships among fluid forces, structural deformation, and macroscopic thrust output.

In response to this need, extensive work has been carried out on rigid-flexible coupling dynamics. Kane et al. [19] studied the dynamics of a cantilever beam attached to a moving base, decomposing the motion of the flexible beam into the large rigid-body motion of the base and the elastic deformation of the beam relative to the base, and introducing nonlinear inertial coupling terms in the description of the deformation field. On this basis, Yang et al. [20] established the equations of a rotating flexible beam using Hamilton's principle and Euler-Bernoulli beam theory, and investigated the

centrifugal stiffening effect and the resulting axial-bending coupling dynamic characteristics. Subsequently, Dangarwala and Nagendra Gopal [21] extended the study to non-uniform cross-sections, considering the coupled free vibration of bending-torsion and bending-stretching. Li and Yao [22] introduced geometric nonlinearity and Coriolis terms for beams with variable cross-sections. Building on these works, some researchers further adopted Timoshenko beam theory to account for shear deformation and rotary inertia in rotating beams [23-25]. However, the aforementioned studies are all confined to pure structural dynamics without considering the effects of fluid loads.

In recent years, some studies have introduced the Morison equation into rotating beam models to account for hydrodynamic effects; however, these models are still based on Euler-Bernoulli kinematic assumptions and do not incorporate transverse shear deformation and rotary inertia [26, 27]. This classical simplification exhibits fatal physical limitations in practical underwater rigid-flexible coupled propulsion scenarios. On the one hand, to withstand large added mass and drag forces, practical propulsors often adopt low-aspect-ratio configurations with finite thickness, where transverse shear deformation is significant and cannot be decoupled from bending [28]. Unlike structural vibrations in the air, the dense underwater environment exerts massive distributed hydrodynamic loads, which severely amplify local shear stresses. Recent fluid-structure interaction analyses confirm that as the slenderness ratio decreases, the transverse shear deformation induced by massive hydrodynamic added mass becomes highly prominent, rendering the predictions of the Euler-Bernoulli model severely inaccurate compared to the Timoshenko framework [29]. On the other hand, efficient maneuvering requires the system to operate over a broad frequency range. During high-frequency maneuvers, the local segments experience rapid reciprocating oscillations, which dramatically amplifies the rotary inertia effect of the cross-section [30]. The coupling of these two factors means that traditional models based on Euler-Bernoulli assumptions cannot accurately capture the high-frequency transient deformation characteristics dominated by shear and rotary inertia [31, 32]. Most crucially, accurate transient thrust prediction relies on precisely projecting local normal hydrodynamic forces onto the global propulsion axis. Because Timoshenko beam theory uniquely

decouples the cross-sectional rotation from the neutral axis deflection, it provides a rigorous spatial slope correction for this force projection. Relying on Euler-Bernoulli assumptions introduces fundamental geometric projection errors, leading to severe computational distortions in the transient thrust response and its magnitude. Therefore, how to simultaneously incorporate the shear deformation and rotary inertia effects of Timoshenko beams and the nonlinear fluid forces described by the Morison equation within a rigid-flexible coupling framework still lacks systematic theoretical investigation, which constitutes the motivation of the present study.

In this study, the kinematic assumptions of Timoshenko beam theory [33, 34] and the Morison equation [35, 36] are simultaneously introduced into a large-amplitude oscillation dynamic framework, establishing a rigid-flexible coupling model that rigorously accounts for transverse shear deformation and cross-sectional rotary inertia and is driven by alternating fluid forces. Based on this theoretical model and a companion underwater oscillatory experimental platform, this paper provides an in-depth analysis of the transient interaction mechanisms between nonlinear hydrodynamic forces and structural deformation, and elucidates the decisive role of the high-frequency transient deformation characteristics induced by transverse shear and rotary inertia in the dynamic modulation of thrust. On this basis, through parametric analyses across different materials and scales, this paper quantitatively reveals the regulation laws of cross-sectional geometric stiffness and driving parameters on propulsion performance, providing a solid theoretical foundation for the optimal design of high-performance flexible propulsors.

The remainder of this paper is organized as follows: Section 2 introduces the kinematic setup of the hub-beam system, establishes the rigid-flexible coupling dynamic equations based on Timoshenko theory, and derives the analytical expression for transient thrust under alternating hydrodynamic forces. Section 3 describes the experimental setup and hydrodynamic calibration, and conducts multi-dimensional validations of the model under various materials, stiffnesses, and driving conditions. Section 4 utilizes the validated model to elucidate the thrust dynamic modulation mechanism of flexible propulsion, and systematically investigates the regulatory laws

of geometric and driving parameters on performance. Section 5 summarizes the conclusions. Appendix A presents a pure rigid-body oscillating propulsion model neglecting elasticity to serve as a baseline for comparison. Appendix B provides the degeneration process of the proposed model to the Euler-Bernoulli beam theory to prove the generality and self-consistency of the theory. Appendix C details the non-dimensionalization derivation process of the governing equations.

2. A Rigid-Flexible Coupling Dynamic Model Based on Timoshenko Beam Theory

In biomimetic BCF propulsion systems, the deformation of the flexible structure that simulates the caudal fin plays a decisive role in thrust generation [10, 37]. To accurately describe the coupling between the large rigid-body rotation of the structure in fluid and its local elastic deformation, this section introduces the Timoshenko beam theory. This theory simultaneously accounts for shear deformation and cross-sectional rotary inertia, and is used here to establish the governing dynamic equations of the hub-flexible beam system.

2.1 Kinematics

This paper considers a hub-beam system model as illustrated in Fig. 1. A uniform beam of length L, width b, height h, density ρ, elastic modulus E, and shear modulus G is fixed to a rigid hub of radius R and mass moment of inertia I_h. The inertial coordinate system O-$X_1X_2X_3$ has base vectors $\boldsymbol{I}$, $\boldsymbol{J}$, and $\boldsymbol{K}$ along the OX_1-, OX_2-, and OX_3-axes, respectively. The hub is connected to an actuator that applies a torque τ to rotate it about the OX_3-axis, and the motion of the beam is constrained to the horizontal O-X_1X_2 plane, where the effect of gravity is assumed to be negligible. Based on the classic floating frame of reference formulation widely employed in flexible multibody dynamics [38], floating coordinate system o-$x_1x_2x_3$ that moves with the beam is established, with base vectors $\boldsymbol{i}$, $\boldsymbol{j}$, and $\boldsymbol{k}$ along the ox_1-, ox_2-, and ox_3-axes, respectively. The x_1-axis coincides with the neutral axis of the undeformed beam. The rotation angle of the floating coordinate system with respect to the inertial coordinate

system is denoted by α.

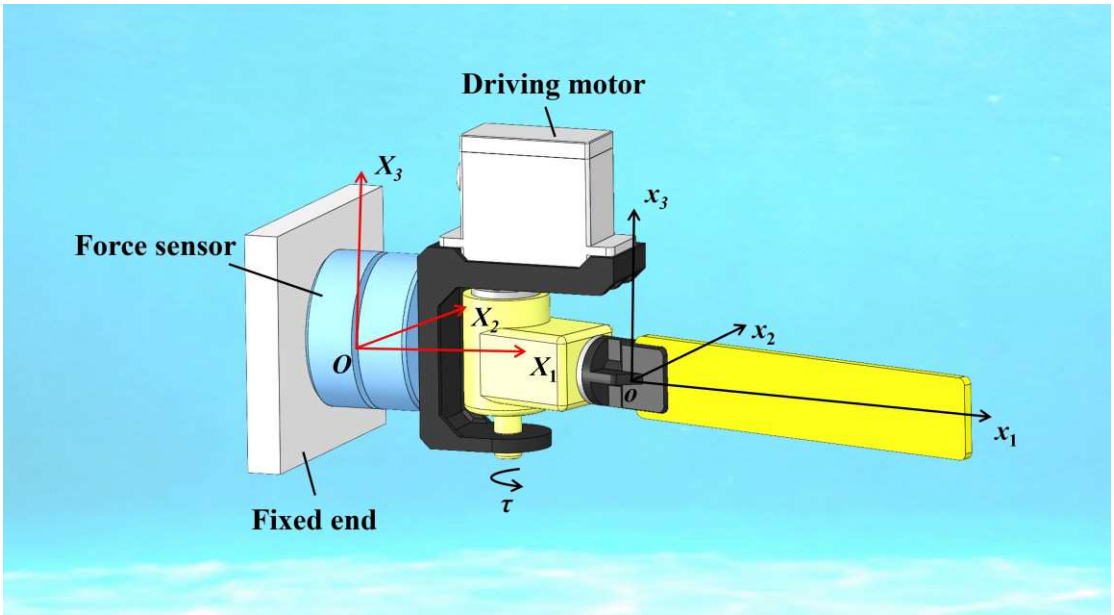


Fig. 1. Hub-beam system.

The base vectors of the inertial coordinate system and the floating coordinate system satisfy the following coordinate transformation relationship:

$$\begin{Bmatrix} \boldsymbol{i} \\ \boldsymbol{j} \end{Bmatrix} = \begin{bmatrix} \cos\alpha & \sin\alpha \\ -\sin\alpha & \cos\alpha \end{bmatrix} \begin{Bmatrix} \boldsymbol{I} \\ \boldsymbol{J} \end{Bmatrix}. \tag{1}$$

To determine the absolute velocity and acceleration of the flexible beam in the subsequent dynamic modeling, taking the first and second derivatives of the above transformation matrix with respect to time t yields the instantaneous kinematic relations of the floating base vectors:

$$\frac{\mathrm{d}\boldsymbol{i}}{\mathrm{d}t} = \dot{\alpha}\boldsymbol{j}, \quad \frac{\mathrm{d}\boldsymbol{j}}{\mathrm{d}t} = -\dot{\alpha}\boldsymbol{i}. \tag{2}$$

Furthermore, one can obtain

$$\frac{\mathrm{d}(\dot{\alpha}\boldsymbol{i})}{\mathrm{d}t} = \ddot{\alpha}\boldsymbol{i} + \dot{\alpha}^2\boldsymbol{j}, \quad \frac{\mathrm{d}(\dot{\alpha}\boldsymbol{j})}{\mathrm{d}t} = -\dot{\alpha}^2\boldsymbol{i} + \ddot{\alpha}\boldsymbol{j}, \tag{3}$$

where $\dot{\alpha}$ and $\ddot{\alpha}$ denote the instantaneous angular velocity and angular acceleration of the large-scale rigid-body rotation of the system, respectively. Additionally, to formulate the virtual displacement associated with the rigid-body rotation for the virtual work principle, it is noted that the base vectors depend intrinsically on the instantaneous rotation angle α. Based on Eq. (1), their partial derivatives with respect to the angle

satisfy:

$$\frac{\partial \boldsymbol{i}}{\partial \alpha} = \boldsymbol{j}, \quad \frac{\partial \boldsymbol{j}}{\partial \alpha} = -\boldsymbol{i}. \tag{4}$$

These kinematic relations of the local frame provide the necessary mathematical basis for deriving the Timoshenko displacement field and computing the virtual work in subsequent sections.

In the floating coordinate system o-$x_1x_2x_3$, the undeformed coordinates of a point on the neutral axis ox_1 of the beam are (x_1, 0, 0). Due to elastic deformation of the beam, based on Timoshenko beam theory, the displacement field after deformation can be expressed as:

$$u(x_1, x_2, t) = u(x_1, t) - x_2\phi(x_1, t), \tag{5a}$$

$$v(x_1, x_2, t) = v(x_1, t), \tag{5b}$$

where $u(x_1, t)$ and $v(x_1, t)$ are the axial and transverse displacements of the neutral axis, respectively, and $\phi(x_1, t)$ is the cross-sectional rotation angle. Unlike the classical Euler-Bernoulli beam theory, the Timoshenko theory accounts for shear deformation; thus, the cross-sectional rotation is independent of the slope of the transverse displacement (i.e., $\phi \neq -\partial v(x_1, t) / \partial x_1$).The position vector $\boldsymbol{r}$ of an arbitrary point on the deformed beam in the inertial frame is:

$$\boldsymbol{r} = [R + x_1 + (u - x_2\phi)]\boldsymbol{i} + (x_2 + v)\boldsymbol{j}. \tag{6}$$

By taking the first derivative of Eq. (6) with respect to time t and substituting the base-vector kinematic relations from Eq. (2), the absolute velocity vector $\boldsymbol{v}$ of the point is obtained:

$$\boldsymbol{v} = [\dot{u} - x_2\dot{\phi} - (x_2 + v)\dot{\alpha}]\boldsymbol{i} + [\dot{v} + (R + x_1 + u - x_2\phi)\dot{\alpha}]\boldsymbol{j}. \tag{7}$$

Taking the derivative of the velocity vector with respect to time again and applying Eq. (3), absolute acceleration vector $\boldsymbol{a}$ is derived as:

$$\begin{aligned} \boldsymbol{a} = {} & [\ddot{u} - x_2\ddot{\phi} - (x_2 + v)\ddot{\alpha} - 2\dot{v}\dot{\alpha} - (R + x_1 + u - x_2\phi)\dot{\alpha}^2]\boldsymbol{i} \\ & + [\ddot{v} - (x_2 + v)\dot{\alpha}^2 + 2(\dot{u} - x_2\dot{\phi})\dot{\alpha} + (R + x_1 + u - x_2\phi)\ddot{\alpha}]\boldsymbol{j}. \end{aligned} \tag{8}$$

Similarly, utilizing the partial derivatives in Eq. (4) and applying the variational

operator to the position vector in Eq. (6), the virtual displacement $\delta \boldsymbol{r}$ can be expressed as:

$$\begin{aligned}\delta \boldsymbol{r} &= \frac{\partial \boldsymbol{r}}{\partial \alpha}\delta\alpha + \frac{\partial \boldsymbol{r}}{\partial u}\delta u + \frac{\partial \boldsymbol{r}}{\partial v}\delta v + \frac{\partial \boldsymbol{r}}{\partial \phi}\delta\phi \\ &= [\delta u - x_2\delta\phi - (x_2 + v)\delta\alpha]\boldsymbol{i} + [(R + x_1 + u - x_2\phi)\delta\alpha + \delta v]\boldsymbol{j}.\end{aligned} \tag{9}$$

2.2 Variational Principle and Governing Equations

Strain

Based on the Timoshenko beam theory, the normal strain ε_{11} and the transverse shear strain ε_{12} are defined by the displacement field as:

$$\varepsilon_{11} = \frac{\partial u}{\partial x_1} - x_2\frac{\partial \phi}{\partial x_1}, \tag{10a}$$

$$\varepsilon_{12} = \frac{1}{2}\left(\frac{\partial v}{\partial x_1} - \phi\right). \tag{10b}$$

Internal Energy

The variation of the strain energy can be expressed in terms of the non-zero stress components σ_{11} and τ_{12} as:

$$\delta U = \int_V (\sigma_{11}\delta\varepsilon_{11} + 2\tau_{12}\delta\varepsilon_{12})\mathrm{d}V. \tag{11}$$

Substituting the strain definitions in Eqs. (10a)-(10b) into Eq. (11) and performing integration by parts over the beam length L, the variation of the strain energy can be expressed in terms of domain and boundary integrals:

$$\delta U = \int_0^L \left(-\frac{\partial N}{\partial x_1}\delta u - \frac{\partial Q}{\partial x_1}\delta v + \left(-Q + \frac{\partial M}{\partial x_1}\right)\delta\phi\right)\mathrm{d}x_1 + [N\delta u + Q\delta v - M\delta\phi]_0^L. \tag{12}$$

where N, M, and Q are the stress resultants over the cross-section A, representing the axial force, the bending moment, and the shear force, respectively. Based on linear elastic material properties, they are explicitly defined in terms of the displacements as:

$$N = \int_A \sigma_{11}\mathrm{d}A = EA\frac{\partial u}{\partial x_1}, \tag{13a}$$

$$M = \int_A \sigma_{11} x_2 \mathrm{d}A = -EI \frac{\partial \phi}{\partial x_1}, \tag{13b}$$

$$Q = \int_A \tau_{12} \mathrm{d}A = k_s GA(\frac{\partial v}{\partial x_1} - \phi), \tag{13c}$$

where k_s is the shear correction factor introduced to account for the non-uniform distribution of the transverse shear stress over the cross-section (Cowper, 1966).

Inertial Force

The virtual work done by the inertial force and the added mass force is considered together. Let $\rho_e = \rho_s + \rho_f C_a$ denote the effective density of the system, where ρ_s is the solid density and C_a is the added mass coefficient. The sum of the virtual work $\delta W_{\text{Add}} + \delta W_{\text{Iner}}$ is given by:

$$\delta W_{\text{Add}} + \delta W_{\text{Iner}} = -\int_V \rho_e \boldsymbol{a} \cdot \delta \boldsymbol{r} \mathrm{d}V. \tag{14}$$

Substituting the absolute acceleration $\boldsymbol{a}$ from Eq. (8) and the virtual displacement $\delta \boldsymbol{r}$ from Eq. (9), and integrating over the cross-sectional area A and the moment of inertia I, we obtain after rearrangement:

$$\begin{aligned} \delta W_{\text{Add}} + \delta W_{\text{Iner}} = -\rho_e \int_0^L \{ & A[\ddot{u} - v\ddot{\alpha} - 2\dot{v}\dot{\alpha} - (R + x_1 + u)\dot{\alpha}^2]\delta u \\ & + A[\ddot{v} - v\dot{\alpha}^2 + 2\dot{u}\dot{\alpha} + (R + x_1 + u)\ddot{\alpha}]\delta v \\ & + I(\ddot{\phi} + \ddot{\alpha} - \phi\dot{\alpha}^2)\delta\phi \\ & + [A(-v\ddot{u} + v^2\ddot{\alpha} + 2v\dot{v}\dot{\alpha}) + A(R + x_1 + u)(\ddot{v} + 2\dot{u}\dot{\alpha}) \\ & + A(R + x_1 + u)^2\ddot{\alpha} + I(\ddot{\phi} + \ddot{\alpha} + 2\phi\dot{\phi}\dot{\alpha} + \phi^2\ddot{\alpha})]\delta\alpha \} \mathrm{d}x_1. \end{aligned} \tag{15}$$

Mechanical Force

Furthermore, the virtual work δW_{Hub} of the inertial force on the rigid hub is formulated as:

$$\delta W_{\text{Hub}} = -I_h \ddot{\alpha} \delta\alpha. \tag{16}$$

where I_h is the mass moment of inertia of the rigid hub, representing the inertial resistance of the driving mechanism as it rotates about the OX_3-axis.The virtual work δW_{Ext} done by the external driving torque can be written as:

$$\delta W_{\text{Ext}} = \tau \delta\alpha. \tag{17}$$

Hydrodynamic Force

The virtual work δW_{Fluid} done by the normal hydrodynamic force can be expressed as:

$$\delta W_{\text{Fluid}} = -\int_S \frac{1}{2}\rho_f C_n \| \boldsymbol{v}_n \| \boldsymbol{v}_n \cdot \delta \boldsymbol{r} \mathrm{d}S, \tag{18}$$

where ρ_f is the fluid density, and C_n is the normal hydrodynamic coefficient. Substituting the normal velocity vector $\boldsymbol{v}_n = \boldsymbol{v}_n \boldsymbol{j}$, where the scalar local normal relative velocity v_n is defined as $v_n = \dot{v} + (R + x_1 + u)\dot{\alpha}$ and the total virtual displacement $\delta \boldsymbol{r}$ from Eq. (9) into the above equation, into the virtual work equation, the orthogonal properties of the base vectors are applied. This automatically eliminates the virtual work contribution from the axial deformation, yielding:

$$\delta W_{\text{Fluid}} = -\frac{1}{2}\rho_f C_n b \int_0^L | v_n | v_n [\delta v + (R + x_1 + u)\delta\alpha] \mathrm{d}x_1. \tag{19}$$

The Generalized Principle of Virtual Work

According to the generalized principle of virtual work, the variation of the strain energy δU equals the total virtual work done by the external and inertial forces:

$$\delta U = \delta W_{\text{Fluid}} + \delta W_{\text{Add}} + \delta W_{\text{Iner}} + \delta W_{\text{Hub}} + \delta W_{\text{Ext}}. \tag{20}$$

Substituting Eq. (12) and the virtual work components into Eq. (20), and applying the fundamental lemma of the calculus of variations, the governing equations expressed in terms of the internal forces are obtained as:

$$\frac{\partial N}{\partial x_1} + \underbrace{\rho_e A[v\ddot{\alpha} + 2\dot{v}\dot{\alpha} + (R + x_1 + u)\dot{\alpha}^2]}_{\text{Axial Fictitious Forces}} = \rho_e A\ddot{u}, \tag{21a}$$

$$\frac{\partial Q}{\partial x_1} + \underbrace{\rho_e A[v\dot{\alpha}^2 - 2\dot{u}\dot{\alpha} - (R + x_1 + u)\ddot{\alpha}]}_{\text{Transverse Fictitious Forces}} - \frac{1}{2}\rho_f C_n b | v_n | v_n = \rho_e A\ddot{v}, \tag{21b}$$

$$Q - \frac{\partial M}{\partial x_1} + \underbrace{\rho_e I(-\ddot{\alpha} + \phi\dot{\alpha}^2)}_{\text{Rotational Fictitious Moments}} = \rho_e I\ddot{\phi}. \tag{21c}$$

$$
\begin{aligned}
&I_h\ddot{\alpha}+\int_0^L \rho_e A[-v\ddot{u}+v^2\ddot{\alpha}+2v\dot{v}\dot{\alpha}+(R+x_1+u)(\ddot{v}+2\dot{u}\dot{\alpha})\\
&+(R+x_1+u)^2\ddot{\alpha}]\mathrm{d}x_1+\int_0^L \rho_e I(\ddot{\phi}+\ddot{\alpha}+2\phi\dot{\phi}\dot{\alpha}+\phi^2\ddot{\alpha})\mathrm{d}x_1\\
&+\int_0^L \frac{1}{2}\rho_f C_n b(R+x_1+u)\,|v_n|\,v_n\mathrm{d}x_1=\tau.
\end{aligned}
\tag{21d}
$$

Among the obtained governing equations, Eqs. (21a)-(21c) dictate the dynamic equilibrium of the flexible beam, while Eq. (21d) governs the global torque balance of the system. Notably, when the first three integral terms on the left-hand side of this equation vanish, it analytically reduces to the classical Euler rotational equation describing rigid-body rotation. In the present study, the driving system imposes a prescribed harmonic oscillation on the rigid hub. Since the rotation angle $\alpha(t)$ is a known kinematic input rather than an unknown degree of freedom, the torque balance equation merely serves as an uncoupled relation to determine the required external driving torque τ. Consequently, it does not need to be solved simultaneously with the structural deformation equations and is thus omitted in the subsequent calculations.

Substituting the constitutive relations, Eqs. (13a)-(13c), into the internal force field equations, Eqs. (21a)-(21c), the displacement-based governing equations for the flexible beam are derived:

$$
EA\frac{\partial^2 u}{\partial x_1^2}-\rho_e A[\ddot{u}-v\ddot{\alpha}-2\dot{v}\dot{\alpha}-(R+x_1+u)\dot{\alpha}^2]=0, \tag{22a}
$$

$$
k_s GA\left(\frac{\partial^2 v}{\partial x_1^2}-\frac{\partial \phi}{\partial x_1}\right)-\rho_e A[\ddot{v}-v\dot{\alpha}^2+2\dot{u}\dot{\alpha}+(R+x_1+u)\ddot{\alpha}]-\frac{1}{2}\rho_f C_n b\,|v_n|\,v_n=0, \tag{22b}
$$

$$
EI\frac{\partial^2 \phi}{\partial x_1^2}+k_s GA\left(\frac{\partial v}{\partial x_1}-\phi\right)-\rho_e I(\ddot{\phi}+\ddot{\alpha}-\phi\dot{\alpha}^2)=0. \tag{22c}
$$

Boundary Conditions

Finally, from the boundary term in Eq. (12), the corresponding boundary conditions for the flexible beam are identified as:

$$
\begin{aligned}
&u\big|_{x_1=0}=0, \qquad v\big|_{x_1=0}=0, \qquad \phi\big|_{x_1=0}=0,\\
&N\big|_{x_1=L}=0, \quad Q\big|_{x_1=L}=0, \quad M\big|_{x_1=L}=0.
\end{aligned}
\tag{23}
$$

The above equations constitute a fully coupled dynamic model of the flexible hub-beam system, which can be further employed to analyze the influence of the beam's flexible

deformation on propulsion performance.

2.3 Bionic Hydrodynamic Analysis and Thrust Calculation

During the intense rigid-flexible coupled dynamic process, the hydrodynamic force is strictly perpendicular to the transient external geometric boundary of the flexible beam [39]. Assume that the initial undeformed neutral axis coincides with the ox_1-axis. At any instant t, the position vector of a differential element on the neutral axis can be expressed as $\boldsymbol{r}(x_1,t)=[x_1+u,v]^{\mathrm{T}}$. By taking the partial derivative of this vector with respect to the initial axial coordinate x_1 and normalizing it, the local tangent vector can be obtained. Rotating this tangent vector counterclockwise by 90° determines the unit normal vector $\boldsymbol{n}(x_1, t)$ that dominates the direction of the fluid action. Since the axial strain $\partial u/\partial x_1$ in this configuration is an infinitesimally small quantity and can be neglected, only retaining the spatial slope of the transverse deformation $\partial v/\partial x_1$, the unit normal vector can be approximately expressed as:

$$\boldsymbol{n}(x_1,t)\approx\frac{1}{\sqrt{1+(\frac{\partial v}{\partial x_1})^2}}[-\frac{\partial v}{\partial x_1},1]^{\mathrm{T}}. \tag{24}$$

The Timoshenko beam theory introduces a shear deformation mechanism, which implies that the cross-sectional rotation angle ϕ is no longer equal to the centerline slope $\partial v/\partial x_1$. Consequently, the deformed cross-section is no longer strictly perpendicular to the neutral axis. However, the hydrodynamic force, dominated by the surface dynamic pressure, only acts on the macroscopic outer surface of the beam. The unique geometric parameter that determines the local angle of attack of the flow field and the spatial direction of the hydrodynamic force is the normal vector $\boldsymbol{n}(x_1, t)$. This direction is entirely determined by the transverse deformation slope $\partial v/\partial x_1$, and is independent of the cross-sectional rotation angle ϕ, which characterizes internal deformation [40]. Based on the Morison equation, the normal hydrodynamic load $f_{\mathrm{Fluid}}(x_1,t)$ acting on the surface of the flexible beam is given by:

$$f_{\text{Fluid}}(x_1,t)=\frac{1}{2}\rho_f bC_n\,|\,v_n\,|\,v_n. \tag{25}$$

Following the geometric nonlinearity in thrust projection established by the large-amplitude elongated-body theory [39], to characterize the geometric mapping relationship of the local normal force onto the global inertial OX_1-axis, a dimensionless thrust projection coefficient η_{X_1} is defined. Under large-scale flexible deformation, this projection coefficient must be strictly formulated as a trigonometric superposition of the hub rotation angle $\alpha(t)$ and the local bending angle $\arctan(\partial v/\partial x_1)$:

$$\eta_{X_1}=\sin(\alpha(t)+\arctan(\frac{\partial v}{\partial x_1})). \tag{26}$$

Expanding the above trigonometric relationship and applying the small-angle approximation, i.e., $\cos(\arctan(\partial v/\partial x_1))\approx 1$ and $\sin(\arctan(\partial v/\partial x_1))\approx \partial v/\partial x_1$, the nonlinear projection coefficient analytically reduces to:

$$\eta_{X_1}\approx \sin\alpha+\frac{\partial v}{\partial x_1}\cos\alpha. \tag{27}$$

The spatial derivative introduces a correction term $(\partial v/\partial x_1)\cos\alpha$. At specific phases of the oscillation cycle, the severe flexible bending causes this term to produce significant opposite-phase compensation, fundamentally altering the macroscopic projection direction of the local hydrodynamic force. Since the modified projection coefficient η_{X_1} is a function of the spatial coordinate x_1, this projection term cannot be extracted outside the integral sign as a constant. Therefore, the actual contribution of the normal hydrodynamic force in the global thrust direction, F_{Fluid,X_1}, must be integrated continuously over the entire domain of the beam length [0, L]:

$$F_{\text{Fluid},X_1}=\frac{1}{2}\rho_f bC_n\int_0^L|\,v_n\,|\,v_n(\sin\alpha+\frac{\partial v}{\partial x_1}\cos\alpha)\mathrm{d}x_1. \tag{28}$$

The inertial thrust component is obtained by projecting the inertial force in the local coordinate system onto the global inertial OX_1-axis. Since the inertial force acts as a body force on the center of mass of the beam element, its geometric mapping is

only influenced by the rigid-body rotation of the hub and does not require surface slope correction. Integrating the projections of the inertial forces in the local x_1 and x_2 directions along the beam length yields:

$$\begin{aligned} F_{\mathrm{Iner},X_1} = &-\rho_e A\cos\alpha\int_0^L[\ddot{u}-v\ddot{\alpha}-2\dot{v}\dot{\alpha}-(R+x_1+u)\dot{\alpha}^2]\mathrm{d}x_1 \\ &+\rho_e A\sin\alpha\int_0^L[\ddot{v}-v\dot{\alpha}^2+2\dot{u}\dot{\alpha}+(R+x_1+u)\ddot{\alpha}]\mathrm{d}x_1. \end{aligned} \tag{29}$$

In summary, the instantaneous total thrust F_X generated by the oscillation of the flexible beam is:

$$\begin{aligned} F_X &= F_{\mathrm{Fluid},X_1} + F_{\mathrm{Iner},X_1} \\ &= \int_0^L\{\frac{1}{2}\rho_f bC_n\,|v_n|\,v_n(\sin\alpha+\frac{\partial v}{\partial x_1}\cos\alpha) \\ &\quad -\rho_e A[\ddot{u}-v\ddot{\alpha}-2\dot{v}\dot{\alpha}-(R+x_1+u)\dot{\alpha}^2]\cos\alpha \\ &\quad +\rho_e A[\ddot{v}-v\dot{\alpha}^2+2\dot{u}\dot{\alpha}+(R+x_1+u)\ddot{\alpha}]\sin\alpha\}\mathrm{d}x_1. \end{aligned} \tag{30}$$

3. Experimental Validation of the Dynamic Model

In this chapter, an underwater rigid-flexible coupled reciprocating oscillation experimental platform is established to quantitatively evaluate the accuracy of the proposed Timoshenko beam dynamic model by measuring the transient force characteristics of flexible beams under various operating conditions. A control variable method is adopted in the validation process to sequentially investigate the predictive accuracy of the theoretical model under different material constitutive properties, cross-sectional stiffnesses, and driving parameters, providing a validated foundation for subsequent mechanism analysis.

3.1 Experimental System

To conduct the model validation experiments, an underwater rotational oscillating platform equipped with a high-precision multi-axis force sensor was constructed (as shown in Fig. 2). The core oscillating device consists of a driving motor and corresponding adapters. During the measurement process, control signals are transmitted to the driving motor, which then drives the experimental beam via the

adapters to perform reciprocating oscillations underwater at a specified frequency and amplitude. As the beam interacts with the fluid, the transient coupled forces generated during the oscillation are simultaneously captured by the force sensor.

Specifically, the platform achieves real-time synchronous acquisition of the thrust force F_X along the OX_1 direction. In both the proposed model and the experimental coordinate system, the positive direction of the OX_1-axis is defined as pointing from the beam root to the free end. Consequently, when the system generates effective forward propulsion, the measured F_X presents as a negative value.

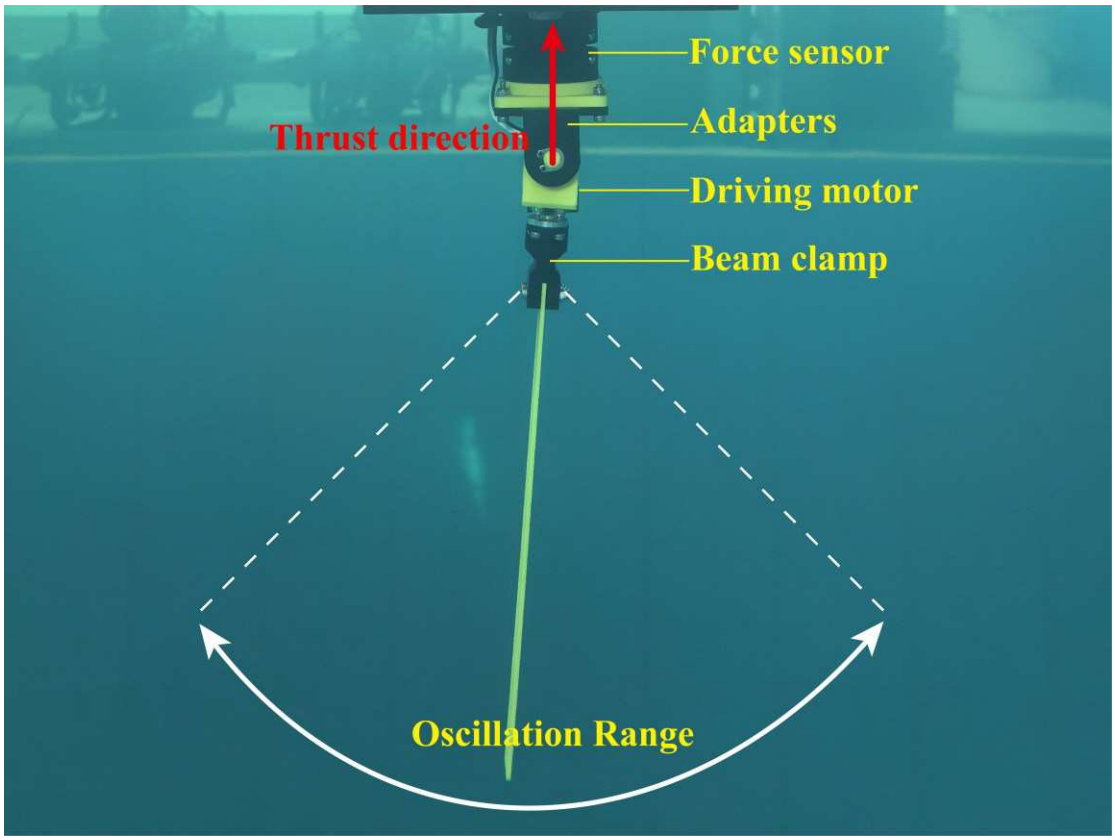


Fig. 2. Experimental setup for the underwater rigid-flexible coupled oscillating system.

3.2 Experimental Specimens and Parameter Setup

The driving system controls the experimental beam to oscillate back and forth around a fixed axis according to a predetermined trajectory. The pitch angle $\alpha(t)$ is defined as:

$$\alpha(t) = B\sin(2\pi ft), \tag{31}$$

where B is the pitching amplitude and f is the driving frequency.

Three sets of specimens were selected for the experiments: a 2-mm-thick polylactic acid (PLA) beam, a 2-mm-thick polymethyl methacrylate (PMMA) beam, and a 5-mm-thick PLA beam, covering different ranges of structural flexibility. The specific mechanical parameters of the specimens are listed in Table 1.

Table 1. Material parameters of the experimental specimens

Material	Density (kg/m^3)	Young's modulus (MPa)	Poisson's ratio
PLA	1170	2850	0.42
PMMA	1150	3400	0.35

In addition, to ensure the consistency of fluid load calculations, the hydrodynamic coefficients were determined through standard flat plate drag experiments in the preliminary stage. The calibrated values, C_n = 2.7291, C_a = 1.4533, are uniformly applied in all theoretical simulations in this chapter and subsequent sections.

3.3 Comparison of Theoretical and Experimental Results under Typical Parameters

To systematically evaluate the predictive accuracy of the proposed Timoshenko rigid-flexible coupled model, the transient thrust F_X was measured under various typical operating conditions and compared with the theoretical predictions. In the presented data plots (e.g., Fig. 3), the shaded regions bounded by the transient curves and the x-axis represent the thrust impulse. The area difference between the red region below the x-axis, indicating forward propulsion, and the blue region above the x-axis, representing reverse drag, intuitively characterizes the effective thrust generated by the system.

First, to verify the theoretical model's capability in predicting the thrust generated by beams of different materials, the driving parameters were fixed at f = 0.6 Hz and B = $\pi/3$ to test 2-mm thick PLA and PMMA beams, respectively.As shown in Fig. 3 for the PLA flexible beam, the theoretical transient thrust agrees well with the experimental measurements. The waveform shifts significantly toward the negative direction, making the red propulsion area below the zero-axis markedly larger than the blue drag area above it, which intuitively demonstrates the generation of effective thrust. When the material is replaced with PMMA (see Fig. 4), the increased stiffness significantly

reduces the degree of waveform asymmetry. This leads to a weakened effective thrust, manifested as a diminished difference between the lower and upper areas, a trend precisely tracked by the theoretical model.

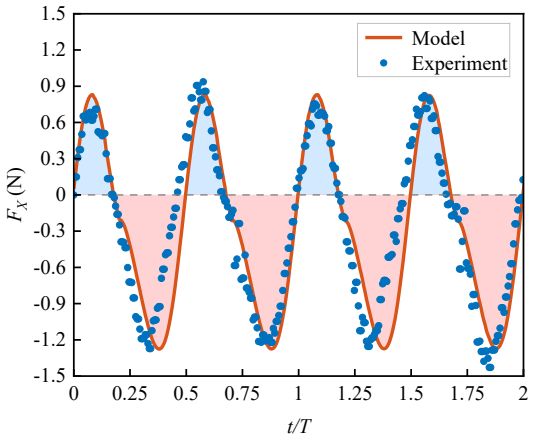


Fig. 3. Comparison of theoretical and experimental transient thrust for the 2-mm PLA beam under baseline conditions ($f = 0.6$ Hz, $B = \pi/3$).

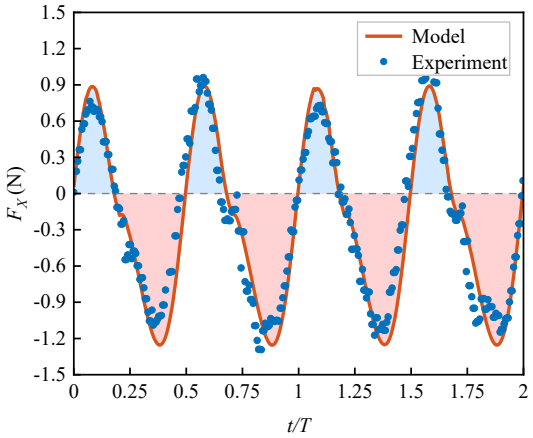


Fig. 4. Transient thrust comparison for the 2-mm PMMA beam under baseline conditions ($f = 0.6$ Hz, $B = \pi/3$).

Second, maintaining the same driving parameters, the model's predictive capability for a beam with greater thickness was verified. By substituting a 5-mm thick PLA beam, the force characteristics exhibit a strictly symmetric oscillation about the zero point. The lower and upper areas perfectly cancel each other out, resulting in an effective thrust converging to zero, as shown in Fig. 5. Under this condition, the model maintains high predictive accuracy, consistent with the rigid-body limit described in Appendix A.

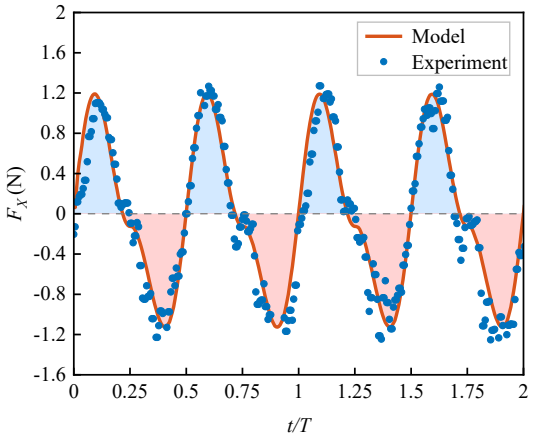


Fig. 5. Transient thrust comparison for the 5-mm PLA beam under baseline conditions (f = 0.6 Hz, B = π/3).

Finally, using the 2-mm PLA beam, the model's predictive capability under different kinematic parameters was validated. Under the low-frequency and large-amplitude condition (f = 0.4 Hz, B = π/3), the positive and negative area distributions are relatively symmetric, yielding a moderate effective thrust, as illustrated in Fig. 6. Conversely, under the high-frequency and small-amplitude condition (f = 0.8 Hz, B = π/6), the waveform undergoes significant asymmetric distortion, as depicted in Fig. 7. The enclosed red area in the negative direction visibly exceeds the blue reverse drag area, indicating high efficiency in effective thrust generation. The theoretical predictions accurately capture these specific nonlinear dynamic area distributions under different external excitations.

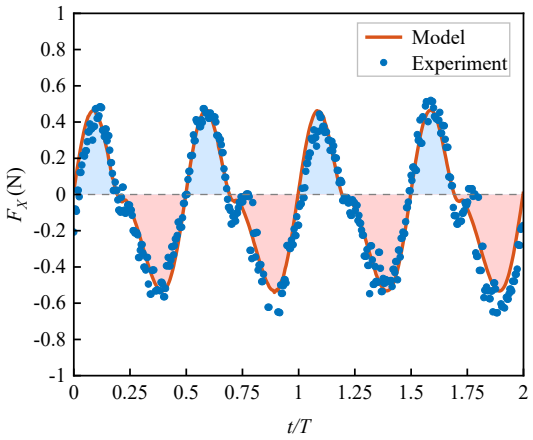


Fig. 6. Transient thrust for the 2-mm PLA beam under low-frequency and large-amplitude conditions (f = 0.4 Hz, B = π/3).

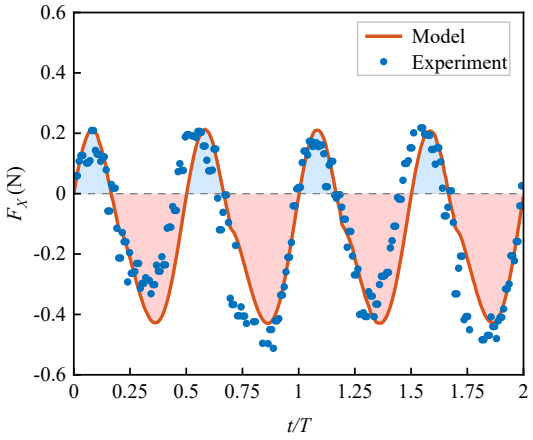


Fig. 7. Transient thrust for the 2-mm PLA beam under high-frequency and small-amplitude conditions (f = 0.8 Hz, B = π/6).

In summary, across variations in material constitutive properties, cross-sectional geometries, and kinematic input conditions, the theoretical calculations exhibit excellent quantitative agreement with the experimental measurements. This demonstrates the accuracy and robustness of the proposed dynamic model, laying a reliable foundation for the in-depth mechanism analysis in the subsequent chapter.

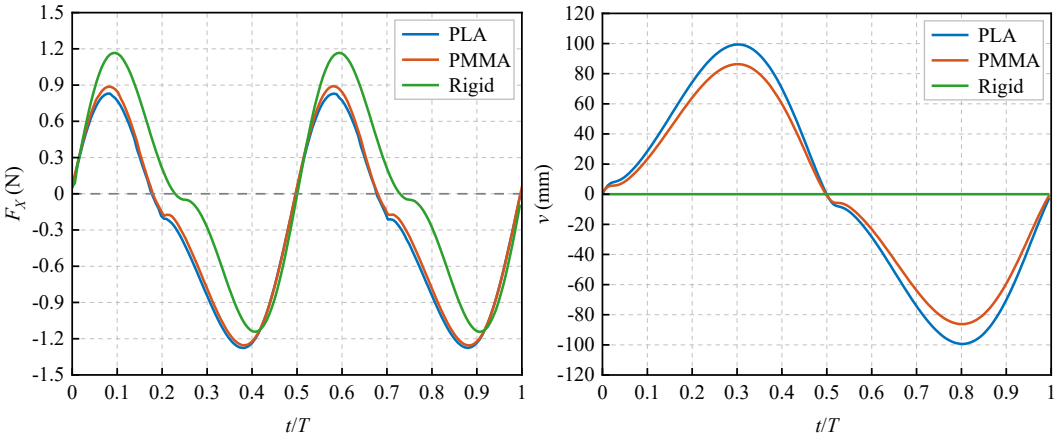
4. Propulsion Mechanism and Parametric Analysis

Based on the previously validated Timoshenko rigid-flexible coupled numerical model, this chapter delves into the core mechanical mechanisms of flexible oscillatory propulsion. Since it is difficult to directly observe the transient stress and local deformation fields within the structure through experimental means, this chapter leverages numerical simulations to dissect the physical roles of structural shear deformation and bending deformation during the rigid-flexible coupled propulsion process driven by hydrodynamic forces. On this basis, a systematic parametric optimization study of cross-sectional geometries and external driving parameters is conducted to provide theoretical guidance for the structural design and operational condition matching of biomimetic BCF propulsors.

4.1 Dynamic Responses under Different Structural Stiffnesses

To elucidate the core mechanical origin of effective propulsion, this section

dissects the causal relationship between structural flexibility, deformation characteristics, and the resulting hydrodynamic forces. Specifically, the dynamic responses of a pure rigid beam, a 2-mm PMMA beam of high stiffness, and a 2-mm PLA beam of moderate flexibility are compared under identical external driving conditions.



(a) (b)

Fig. 8. Dynamic responses under baseline conditions with varying structural stiffness: (a) transient thrust F_X; (b) tip deflection v.

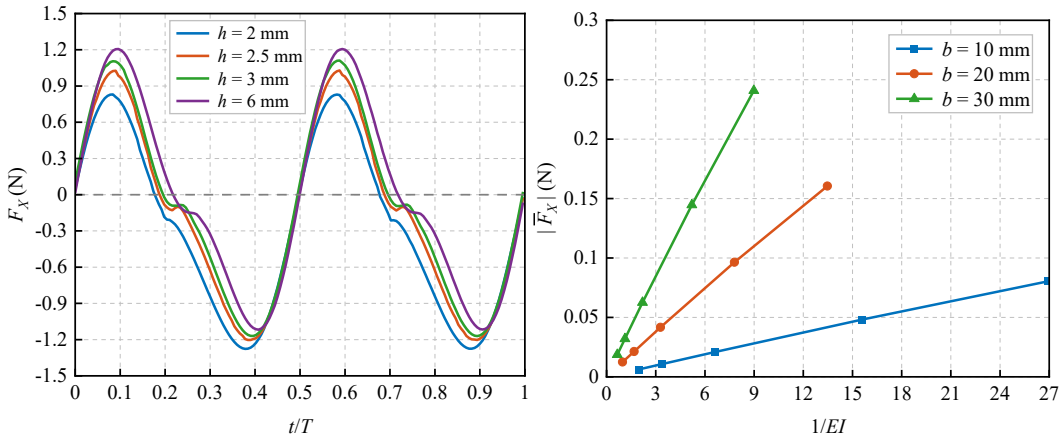
Figure 8(a) illustrates the transient thrust evolution for the three different structural stiffnesses. For the pure rigid beam, the absence of internal elastic deformation forces the local kinematic parameters to maintain strict synchronous symmetry with the driving input. Consequently, the work done by the hydrodynamic loads in the first half-cycle is completely negated by that in the second half-cycle, resulting in a perfectly symmetric thrust waveform and a zero net effective thrust. However, the introduction of structural flexibility breaks this mechanical symmetry. As the material shifts from PMMA to PLA, the structural compliance increases, causing the transient thrust waveform to undergo a progressive and significant distortion toward the negative propulsion direction. This clearly demonstrates that appropriate flexibility is the fundamental prerequisite for transforming symmetric fluid resistance into an asymmetric, effective forward propulsive force, a mechanism that perfectly aligns with the macroscopic experimental observations presented in Section 3.

To further reveal the underlying physical cause of this thrust asymmetry, Fig. 8(b)

extracts the corresponding tip deflection curves , representing the transverse bending deformation, for the three configurations over a stable kinematic cycle. Under the alternating hydrodynamic forces, the pure rigid beam exhibits zero local elastic deflection, maintaining a flat zero line. The PMMA beam, constrained by its higher elastic modulus, experiences a moderate transverse deflection with a peak amplitude of approximately 80 mm. In contrast, the PLA beam exhibits a pronounced, large-scale bending deformation, with its tip deflection reaching nearly 100 mm. During the rigid-flexible coupling process, this flexibility-induced large deformation continuously alters the instantaneous angle of attack of the fluid loads. It is precisely this asymmetric geometric reshaping that fundamentally redirects the macroscopic projection of the local normal hydrodynamic forces toward the longitudinal propulsion axis, thereby effectively changing the thrust characteristics and enhancing the overall propulsion efficiency.

4.2 Effect of Flexibility on Thrust

The geometric dimensions of the cross-section dictate the structural flexural rigidity (EI), which inversely defines the flexibility ($1/EI$) of the propulsor. With a fixed beam length $L = 200$ mm, baseline operating parameters ($f = 0.6$ Hz, $B = \pi/3$), and PLA material, the system performance was systematically analyzed by varying the beam height (thickness) h and width b (see Fig. 9).



(a) (b)

Fig. 9. Effect of cross-sectional geometry on propulsion: (a) transient thrust F_X for

varying beam thicknesses h; (b) absolute average thrust $|\bar{F}_X|$ versus structural flexibility $1/EI$.

Figure 9(a) illustrates the transient thrust F_X waveforms under different beam thicknesses h. When the thickness is relatively large (h = 6 mm), the substantial cross-sectional stiffness severely suppresses elastic deformation. Under this condition, the motion degenerates toward the rigid-body limit, resulting in a nearly symmetric thrust waveform where the positive and negative work done by hydrodynamic loads essentially cancel each other out. As the thickness h decreases, the structural flexibility increases, causing the transient thrust waveform to undergo a progressive and significant asymmetric distortion toward the negative propulsion direction. This transient analysis further confirms that an adequate deformation margin is the fundamental prerequisite for generating effective forward thrust.

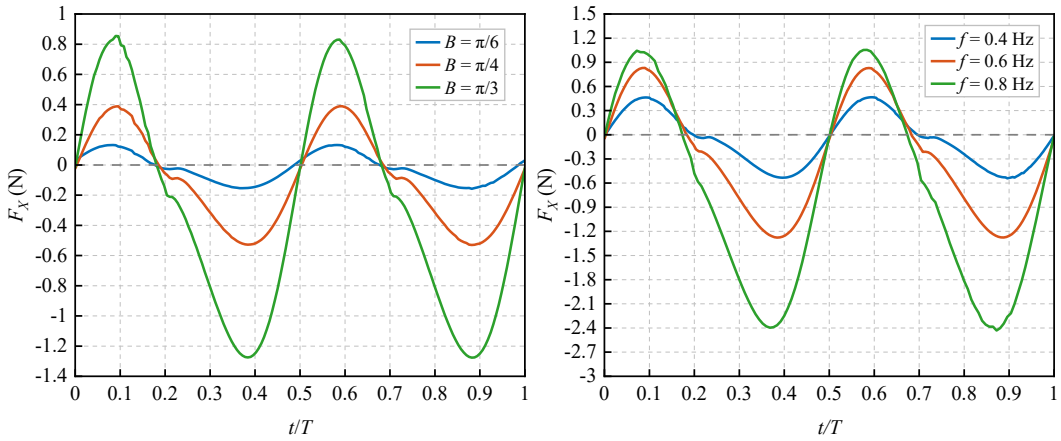
To quantitatively evaluate the macroscopic propulsion performance, Fig. 9(b) demonstrates the variation of the absolute average thrust $|\bar{F}_X|$ as a function of the structural flexibility ($1/EI$) across different beam widths b. The results indicate that the average propulsive force exhibits a nearly linear positive correlation with structural flexibility. The flexibility-induced asymmetric bending mechanism leads to a proportional, monotonic increase in the effective thrust. Furthermore, in the transverse dimension, an increase in the beam width b expands the effective wetted area for hydrodynamic loads. As clearly depicted in Fig. 9(b), a larger width b not only increases the absolute thrust but also significantly steepens the slope of the thrust-flexibility curve. This analysis reveals that enhancing structural flexibility within the material's elastic limit, combined with appropriately increasing the effective hydrodynamic area, constitutes a fundamental rule for the geometric optimization of such flexible propulsors.

4.3 Effect of Kinematic Parameters on Thrust

After clarifying the regulatory mechanisms of the structural properties, it is necessary to further elucidate the influence of kinematic inputs on the rigid-flexible

coupled dynamic responses, particularly to explore the unique dynamic characteristics revealed by the Timoshenko model under high-frequency excitation. Based on the 2-mm PLA beam model, the transient thrust responses under different pitching amplitudes ($B = \pi/6, \pi/4, \pi/3$) and driving frequencies ($f = 0.4, 0.6, 0.8$ Hz) were calculated.

As shown in Fig. 10, with an increase in pitching amplitude B (Fig. 10(a)) or driving frequency f (Fig. 10(b)), the peak and valley values of the transient thrust curves rise sharply, and the overall waveforms shift significantly toward the negative (forward propulsion) direction. According to the applied hydrodynamic model, larger amplitudes and higher frequencies directly lead to a substantial increase in the local oscillating velocity and acceleration of the beam. Because the fluid drag is proportional to the square of the velocity and the added mass force is proportional to the acceleration, these enhanced kinematic inputs excite intense nonlinear hydrodynamic loads, resulting in a notable increase in the absolute amplitude of the effective propulsive force.



(a) (b)

Fig. 10. Transient thrust responses of the 2-mm PLA beam under varying kinematic inputs: (a) varying pitching amplitudes B ($f = 0.6$ Hz); (b) varying driving frequencies f ($B = \pi/3$).

It is particularly noteworthy that under the high-frequency condition ($f = 0.8$ Hz, as clearly seen in Fig. 10(b)), the transient thrust waveform exhibits significant nonlinear distortion and amplitude enhancement. This dynamic feature precisely highlights the core value of employing the Timoshenko beam theory over the traditional Euler-Bernoulli beam theory in this study. Under high-frequency excitation, the inertial

effect of the cross-sectional rotary inertia is significantly amplified, while the transverse shear deformation of the local segments increases sharply. These combined effects, dominated by rotary inertia and transverse shear, profoundly alter the transient dynamic responses and the effective thrust generation under intense hydrodynamic loads. These analytical results prove that within the complex parameter space of high-frequency kinematics, one must rely on a comprehensive dynamic model that incorporates both shear deformation and rotational inertia to achieve precise predictions of the transient propulsion characteristics.

5. Conclusion

In this study, a rigid-flexible coupling dynamic model based on Timoshenko beam theory is established to investigate biomimetic propulsion. The model systematically integrates transient hydrodynamic forces with internal shear deformation and cross-sectional rotary inertia. This approach successfully overcomes the limitations of the classical Euler-Bernoulli theory when applied to stubby appendages and high-frequency oscillations. The theoretical framework was rigorously validated through underwater experiments across various structural stiffnesses and driving parameters.

The results show that forward propulsion relies on the rigid-flexible coupling to break the dynamic symmetry of alternating hydrodynamic forces. The structural bending dynamically alters the local angle of attack. This continuous reshaping asymmetrically reconstructs the fluid forces along the propulsion axis, thereby generating net thrust. Furthermore, parametric analyses reveal clear geometric scaling laws. While excessive beam thickness severely suppresses beneficial elastic deformation ($EI \propto h^3$), identifying an optimal stiffness is crucial to maximize thrust. In contrast, increasing the beam width linearly enhances propulsion by expanding the effective wetted area.

Crucially, the Timoshenko framework captures unique dynamic responses under rapid excitations. By decoupling cross-sectional rotation from neutral axis deflection, the model eliminates the geometric projection errors inherent in the Euler-Bernoulli

assumption. Under high-frequency kinematics, cross-sectional rotary inertia and transverse shear deformation are significantly amplified. These effects not only alter the transient thrust waveform but also ensure a precise spatial slope correction when projecting fluid forces onto the global axis. Ultimately, incorporating shear and rotary inertia is physically indispensable for accurately predicting rigid-flexible coupled dynamics under extreme hydrodynamic loads.

Declaration of Competing Interest

The authors declare that they have no known competing financial interests or personal relationships that could have appeared to influ ence the work reported in this paper.

Data Availability

The datasets generated during and/or analysed during the current study are not publicly available but are available from the corresponding author on reasonable request.

Acknowledgements

This work is supported by the National Natural Science Foundation of China [Grant No. 52401391], the Young Elite Scientists Sponsorship Program by CAST [Grant No. YESS20240453], the Ningbo Yongjiang Talent Program [Grant No. 2024A-179-G], the “Innovation Yongjiang 2035” Key R&D Program [Grant No.2024T001], the China Postdoctoral Science Foundation [Grant No. 2025T181165 and No. 2023M732863], the Fundamental Research Funds for the Central Universities [Grant No. ZDGC03 and No. D5000260457].

Appendix A. Rigid-Body Baseline Model

To facilitate a comparative analysis of the enhancement effect of flexible deformation on propulsion performance, a completely rigid beam model without any

elastic deformation is constructed in this paper as a theoretical baseline. Under the rigid assumption, there is no relative displacement between any infinitesimal elements within the beam, and the displacement field components satisfy $u = v = \phi = 0$. The position vector $\boldsymbol{r}$ of an arbitrary point on the neutral axis of the beam simplifies in the inertial frame to:

$$\boldsymbol{r} = (R + x_1)\boldsymbol{i} + x_2\boldsymbol{j}. \tag{A.1}$$

Utilizing the base-vector kinematic relations, the absolute velocity $\boldsymbol{v}$ and acceleration $\boldsymbol{a}$ of an arbitrary point on the beam are derived respectively as:

$$\boldsymbol{v} = -x_2\dot{\alpha}\boldsymbol{i} + (R + x_1)\dot{\alpha}\boldsymbol{j}, \tag{A.2}$$

$$\boldsymbol{a} = [-x_2\ddot{\alpha} - (R + x_1)\dot{\alpha}^2]\boldsymbol{i} + [-x_2\dot{\alpha}^2 + (R + x_1)\ddot{\alpha}]\boldsymbol{j}. \tag{A.3}$$

Based on the partial derivatives of the base vectors with respect to the rotation angle α, the virtual displacement $\delta\boldsymbol{r}$ is formulated as:

$$\delta\boldsymbol{r} = -x_2\delta\alpha\boldsymbol{i} + (R + x_1)\delta\alpha\boldsymbol{j}. \tag{A.4}$$

The differential hydrodynamic force acting on the rigid beam is described by the Morison equation, comprising the normal hydrodynamic force $\mathrm{d}F_{\mathrm{Fluid}}$ and the added mass force $\mathrm{d}F_{\mathrm{Add}}$. Additionally, the inertial force $\mathrm{d}F_{\mathrm{Iner}}$ arising from the mass distribution must be accounted for:

$$\mathrm{d}F_{\mathrm{Fluid}} = -\frac{1}{2}\rho_f C_n \| \boldsymbol{v}_n \| \boldsymbol{v}_n \mathrm{d}S, \tag{A.5}$$

$$\mathrm{d}F_{\mathrm{Add}} + \mathrm{d}F_{\mathrm{Iner}} = -(\rho_f C_a + \rho_s)\boldsymbol{a}\mathrm{d}V = -\rho_e\boldsymbol{a}\mathrm{d}V, \tag{A.6}$$

where $\boldsymbol{v}_n = \left(R + x_1\right)\dot{\alpha}\boldsymbol{j}$ denotes the normal velocity component.Integrating the virtual work done by these differential forces, along with the virtual work from the hub inertia $\delta W_{\mathrm{Hub}} = -I_h\ddot{\alpha}\delta\alpha$ and the external torque $\delta W_{\mathrm{Ext}} = \tau\delta\alpha$, the total virtual work equation $\delta W_{\mathrm{total}} = 0$ yields the rigid-body equation of motion:

$$\{\rho_e IL + \frac{1}{3}\rho_e A[(R + L)^3 - R^3] + I_h\}\ddot{\alpha} + \frac{1}{8}\rho_f C_n b | \dot{\alpha} | \dot{\alpha}[(R + L)^4 - R^4] = \tau. \tag{A.7}$$

The instantaneous thrust F_X generated by the rigid beam along the inertial OX_1-axis is the sum of the projections of the normal hydrodynamic force and the inertial force. Applying the coordinate transformation $\boldsymbol{i}\cdot\boldsymbol{I}=\cos\alpha$ and $\boldsymbol{j}\cdot\boldsymbol{I}=-\sin\alpha$, the thrust evaluates to:

$$\begin{aligned} F_X = &\frac{1}{6}\rho_f b C_n \sin\alpha\,|\dot{\alpha}|\dot{\alpha}[(R+L)^3-R^3] \\ &+\frac{1}{2}\rho_e A(\dot{\alpha}^2\cos\alpha+\ddot{\alpha}\sin\alpha)[(R+L)^2-R^2]. \end{aligned} \tag{A.8}$$

Appendix B. Degeneration to the Euler-Bernoulli Beam Model

This appendix presents the detailed analytical procedure by which the Timoshenko beam model established in this paper degenerates to the classical Euler-Bernoulli beam model when transverse shear deformation and cross-sectional rotary inertia are neglected. Under the classical Euler-Bernoulli beam assumption, the cross-section remains plane and strictly perpendicular to the neutral axis after deformation. This imposes the geometric constraint $\phi=\partial v/\partial x_1$. Consequently, the transverse shear strain ε_{12} vanishes identically:

$$\varepsilon_{12}=\frac{\partial v}{\partial x_1}-\phi=0. \tag{B.1}$$

Substituting this geometric constraint into the normal strain definition, the axial normal strain degenerates to:

$$\varepsilon_{11}=\frac{\partial u}{\partial x_1}-x_2\frac{\partial^2 v}{\partial x_1^2}. \tag{B.2}$$

The axial equation of motion, Eq. (22a), does not contain shear force or rotary inertia terms; therefore, its structural form remains invariant during the degeneration process. For the transverse vibration, enforcing the geometric constraint $\phi=\partial v/\partial x_1$ causes the shear force constitutive term $Q=k_sGA(\partial v/\partial x_1-\phi)$ to approach zero. Furthermore, by neglecting the rotary inertia term $\rho_e I\ddot{\phi}$, the governing equation for

the cross-sectional rotation, Eq. (22c), simplifies to an explicit expression for the internal shear force:

$$EI\frac{\partial^3 v}{\partial x_1^3}+Q=0. \tag{B.3}$$

Differentiating this relation with respect to x_1 yields $\partial Q/\partial x_1=-EI(\partial^4 v/\partial x_1^4)$. Substituting this relationship into the transverse equation of motion, Eq. (22b), to eliminate the shear force gradient, yields the classical Euler-Bernoulli flexural vibration equation coupled with the large-scale rigid-body rotation:

$$\begin{aligned}&-EI\frac{\partial^4 v}{\partial x_1^4}+\underbrace{\rho_e A[v\dot{\alpha}^2-2\dot{u}\dot{\alpha}-(R+x_1+u)\ddot{\alpha}]}_{\text{Transverse Fictitious Forces}}\\&-\frac{1}{2}\rho_f C_n b\,|\dot{v}+(R+x_1+u)\dot{\alpha}|\,[\dot{v}+(R+x_1+u)\dot{\alpha}]=\rho_e A\ddot{v}\end{aligned} \tag{B.4}$$

Finally, substituting the kinematic relation $\phi=\partial v/\partial x_1$ into the original Timoshenko boundary conditions, Eq. (23), naturally yields the classical Euler-Bernoulli boundary conditions:

$$\begin{aligned}&u\big|_{x_1=0}=0,\quad v\big|_{x_1=0}=0,\quad \left.\frac{\partial v}{\partial x_1}\right|_{x_1=0}=0,\\&N\big|_{x_1=L}=0,\quad Q\big|_{x_1=L}=0,\quad M\big|_{x_1=L}=0.\end{aligned} \tag{B.5}$$

This consistent degeneration verifies the mathematical generality and self-consistency of the rigid-flexible coupling model established in this paper.

Appendix C. Non-dimensionalization of the Governing Equations

To effectively account for scaling and size effects in solid mechanics analysis, the rigid-flexible coupled dynamic governing equations must be non-dimensionalized. This procedure eliminates scale-dependent physical parameters and introduces dimensionless quantities, laying a solid foundation for subsequent numerical simulations. Let ω be the characteristic angular frequency of the hub actuator's motion. The following dimensionless parameters are introduced:

$$\bar{t}=\omega t,\quad \dot{(\,)}=\frac{\partial(\,)}{\partial\bar{t}},\quad \ddot{(\,)}=\frac{\partial^2(\,)}{\partial\bar{t}^2}, \tag{C.1a}$$

$$\bar{u}=\frac{u}{L},\quad \bar{v}=\frac{v}{L},\quad \bar{x}_1=\frac{x_1}{L},\quad \bar{R}=\frac{R}{L},\quad \bar{b}=\frac{b}{L},\quad \bar{h}=\frac{h}{L}, \tag{C.1b}$$

$$\frac{\partial}{\partial x_1}=\frac{1}{L}\frac{\partial}{\partial \bar{x}_1},\quad \frac{\partial^2}{\partial x_1^2}=\frac{1}{L^2}\frac{\partial^2}{\partial \bar{x}_1^2}, \tag{C.1c}$$

$$\bar{A}=\frac{A}{L^2},\quad \bar{I}=\frac{I}{L^4},\quad \bar{\rho}_f=\frac{\rho_f}{\rho_s},\quad \bar{\rho}_e=\frac{\rho_e}{\rho_s}, \tag{C.1d}$$

$$\bar{E}=\frac{E}{\rho_s\omega^2L^2},\quad \bar{G}=\frac{G}{\rho_s\omega^2L^2}. \tag{C.1e}$$

Substituting the above dimensionless parameters into the governing equations, Eqs. (22a)-(22c), yields the dimensionless forms of the axial and transverse equations of motion:

$$\bar{E}\bar{A}\frac{\partial^2\bar{u}}{\partial\bar{x}_1^2}-\bar{\rho}_e\bar{A}[\ddot{\bar{u}}-\bar{v}\ddot{\alpha}-2\dot{\bar{v}}\dot{\alpha}-(\bar{R}+\bar{x}_1+\bar{u})\dot{\alpha}^2]=0, \tag{C.2}$$

$$k_s\bar{G}\bar{A}(\frac{\partial^2\bar{v}}{\partial\bar{x}_1^2}-\frac{\partial\phi}{\partial\bar{x}_1})-\bar{\rho}_e\bar{A}[\ddot{\bar{v}}-\bar{v}\dot{\alpha}^2+2\dot{\bar{u}}\dot{\alpha}+(\bar{R}+\bar{x}_1+\bar{u})\ddot{\alpha}]-\frac{1}{2}\bar{\rho}_fC_n\bar{b}\,|\bar{v}_n|\,\bar{v}_n=0. \tag{C.3}$$

where $\bar{v}_n=\frac{v_n}{L\omega}=\dot{\bar{v}}+(\bar{R}+\bar{x}_1+\bar{u})\dot{\alpha}$ denotes the dimensionless local normal relative velocity of the flexible beam. The dimensionless governing equation for the cross-sectional rotation angle is expressed as:

$$\bar{E}\bar{I}\,\frac{\partial^2\phi}{\partial\bar{x}_1^2}+k_s\bar{G}\bar{A}(\frac{\partial\bar{v}}{\partial\bar{x}_1}-\phi)-\bar{\rho}_e\bar{I}\,[\ddot{\phi}+\ddot{\alpha}-\phi\dot{\alpha}^2]=0. \tag{C.4}$$

The dimensionless dynamic boundary conditions correspondingly degenerate to:

$$\begin{aligned}&\bar{u}\big|_{\bar{x}_1=0}=0,\qquad \bar{v}\big|_{\bar{x}_1=0}=0,\qquad \phi\big|_{\bar{x}_1=0}=0,\\ &\left.\frac{\partial\bar{u}}{\partial\bar{x}_1}\right|_{\bar{x}_1=1}=0,\quad \left.(\frac{\partial\bar{v}}{\partial\bar{x}_1}-\phi)\right|_{\bar{x}_1=1}=0,\quad \left.\frac{\partial\phi}{\partial\bar{x}_1}\right|_{\bar{x}_1=1}=0.\end{aligned} \tag{C.5}$$

Similarly, the dimensionless driving torque $\bar{\tau}$ required for the rotational motion is derived as:

$$
\begin{aligned}
\bar{\tau} &= \frac{\tau}{\rho_s L^5 \omega^2} \\
&= \bar{I}_h \ddot{\alpha} + \int_0^1 \{\bar{\rho}_e \bar{A}[-\bar{v}\ddot{\bar{u}} + \bar{v}^2 \ddot{\alpha} + 2\dot{\bar{v}}\dot{\alpha} \\
&+ (\bar{R} + \bar{x}_1 + \bar{u})(\ddot{\bar{v}} + 2\dot{\bar{u}}\dot{\alpha} + \ddot{\alpha}(\bar{R} + \bar{x}_1 + \bar{u}))] \\
&+ \bar{\rho}_e \bar{I}[\ddot{\phi} + (1+\phi^2)\ddot{\alpha} + 2\phi\dot{\phi}\dot{\alpha}] \\
&+ \frac{1}{2}\bar{\rho}_f C_n \bar{b}(\bar{R} + \bar{x}_1 + \bar{u}) \,|\, \bar{v}_n \,|\, \bar{v}_n \} \mathrm{d}\bar{x}_1,
\end{aligned}
\tag{C.6}
$$

where $\bar{I}_h = I_h / (\rho_s L^5)$ denotes the dimensionless hub mass moment of inertia. Finally, the dimensionless instantaneous thrust $\bar{F}_X$ is calculated as follows:

$$
\begin{aligned}
\bar{F}_X &= \frac{F_X}{\rho_s L^4 \omega^2} \\
&= \int_0^1 \{\frac{1}{2}\bar{\rho}_f \bar{b} C_n \,|\, \bar{v}_n \,|\, \bar{v}_n (\sin\alpha + \frac{\partial \bar{v}}{\partial \bar{x}_1}\cos\alpha) \\
&- \bar{\rho}_e \bar{A}[\ddot{\bar{u}} - \bar{v}\ddot{\alpha} - 2\dot{\bar{v}}\dot{\alpha} - (\bar{R} + \bar{x}_1 + \bar{u})\dot{\alpha}^2]\cos\alpha \\
&+ \bar{\rho}_e \bar{A}[\ddot{\bar{v}} - \bar{v}\dot{\alpha}^2 + 2\dot{\bar{u}}\dot{\alpha} + (\bar{R} + \bar{x}_1 + \bar{u})\ddot{\alpha}]\sin\alpha \} \mathrm{d}\bar{x}_1.
\end{aligned}
\tag{C.7}
$$

The above dimensionless equations constitute the complete mathematical model of the flexible hub-beam system. In the next section, numerical simulations will be performed based on this model and compared with experimental measurements for validation.

References

1. Sfakiotakis, M., Lane, D.M., Davies, J.B.C.: Review of fish swimming modes for aquatic locomotion. IEEE J. Oceanic Eng. 24, 237–252 (1999)
2. Tian, Q., Wang, T., Wang, Y., Li, C., Liu, B.: Robust Optimization Design for Path Planning of Bionic Robotic Fish in the Presence of Ocean Currents. J. Mar. Sci. Eng. 10, 1109 (2022)
3. Dharmdas, A., Patil, A.Y., Baig, A., Hosmani, O.Z., Mathad, S.N., Patil, M.B., Kumar, R., Kottursheltar, B.B., Fattah, I.M.: An Experimental and Simulation Study of the Active Camber Morphing Concept on Airfoils Using Bio-Inspired Structures. Biomimetics 8, 251 (2023)

4. Qu, Y., Zhou, Z., Chen, L., Lian, H., Li, X., Hu, Z., Cao, Y., Pan, G.: Uncertainty quantification of vibro-acoustic coupling problems for robotic manta ray models based on deep learning. Ocean Eng. 299, 117388 (2024)
5. Zhang, G., Mei, Y., Mi, C., Pan, E., Qu, Y.: A rigid-flexible dynamic model of flexoelectric robotic metamaterials with large in-plane motions. Int. J. Mech. Sci. 287, 109943 (2025)
6. Zhang, S., Xie, X., Sui, Y., Qu, Y., Zheng, G., Deng, Z.: Dynamic modeling and stiffness optimization for a manta ray-inspired robot. Int. J. Mech. Sci. 316, 111417 (2026)
7. Hussein, A.A., Ragab, S.A., Hajj, M.R., Patil, M.J.: Material and geometric effects on propulsion of a fish tail. Bioinspir. Biomim. 16, 066008 (2021)
8. Mitin, I., Korotaev, R., Ermolaev, A., Mironov, V., Lobov, S.A., Kazantsev, V.B.: Bioinspired Propulsion System for a Thunniform Robotic Fish. Biomimetics 7, 215 (2022)
9. Alqaleiby, H., Hajj, M.R.: Thrust-efficiency limits of a swimming tail with variable chordwise flexural rigidity. Sci. Rep. 15, 4471 (2025)
10. Reddy S., Sen, S., Har, C.: Effect of flexural stiffness distribution of a fin on propulsion performance. Mech. Mach. Theory 129, 218–231 (2018)
11. Kumar, S., McHenry, M.J., Seo, J.-H., Mittal, R.: Flow-induced dorso-ventral deformation enhances propulsive efficiency in flexible caudal fins. Bioinspir. Biomim. 21, 016027 (2026)
12. Zhou, M., Luo, M., Wu, Z., Yang, C.: Fluid-structure interaction analysis for yaw stability and propulsion of the biomimetic fish considering recoil motion. J. Fluids Struct. 142, 104518 (2026)
13. Qu, Y., Xie, X., Zhang, S., Xing, C., Cao, Y., Cao, Y., Pan, G., Song, B.: A Rigid-Flexible Coupling Dynamic Model for Robotic Manta with Flexible Pectoral Fins. J. Mar. Sci. Eng. 12, 292 (2024)
14. Kancharala, A.K., Philen, M.K.: Study of flexible fin and compliant joint stiffness on propulsive performance: theory and experiments. Bioinspir. Biomim. 9, 036011 (2014)

15. Quinn, D.B., Lauder, G.V., Smits, A.J.: Scaling the propulsive performance of heaving flexible panels. J. Fluid Mech. 738, 250–267 (2014)
16. Bhamra, N.S., Vijayan, K.: Underwater bio-inspired propulsion using actuation of coupled structures. Ocean Eng. 331, 121351 (2025)
17. Cui, Z., Jiang, H.: Design and implementation of thunniform robotic fish with variable body stiffness. Int. J. Robot. Autom. 32 (2017)
18. Zhong, Q., Zhu, J., Fish, F.E., Kerr, S.J., Downs, A.M., Bart-Smith, H., Quinn, D.B.: Tunable stiffness enables fast and efficient swimming in fish-like robots. Sci. Robot. 6, eabe4088 (2021)
19. Kane, T.R., Ryan, R.R., Banerjeer, A.K.: Dynamics of a cantilever beam attached to a moving base. J. Guid. Control. Dyn. 10, 139–151 (1987)
20. Yang, J.B., Jiang, L.J., Chen, D.C.: Dynamic modelling and control of a rotating Euler–Bernoulli beam. J. Sound. Vib. 274, 863–875 (2004)
21. Dangarwala, R.K., Nagendra Gopal, K.V.: Coupled free vibration analysis of rotating non-uniform cantilever beams by an element-wise Ritz method using local hierarchical functions. Comput. Struct. 288, 107133 (2023)
22. Li, H., Yao, G.: Nonlinear forced vibration and stability analysis of a rotating three-dimensional cantilever beam with variable cross-section. Thin-Walled Struct. 211, 113104 (2025)
23. Han, H., Liu, L., Cao, D.: Dynamic modeling for rotating composite Timoshenko beam and analysis on its bending-torsion coupled vibration. Appl. Math. Model. 78, 773–791 (2020)
24. Liu, X., Sun, C., Ranjan Banerjee, J., Dan, H.-C., Chang, L.: An exact dynamic stiffness method for multibody systems consisting of beams and rigid-bodies. Mech. Syst. Signal Process. 150, 107264 (2021)
25. Xu, J., Yang, Z., Yang, J., Li, Y.: Influence of the boundary relaxation on the free vibration of rotating composite laminated Timoshenko beams. Compos. Struct. 266, 113690 (2021)

26. Shahab, S., Erturk, A.: Electrohydroelastic Euler–Bernoulli–Morison model for underwater resonant actuation of macro-fiber composite piezoelectric cantilevers. Smart Mater. Struct. 25, 105007 (2016)
27. Xu, C., Sun, Z., Mei, Y., Li, P., Pan, E., Qu, Y.: Rigid-flexible coupling dynamics for bionic body-caudal-fin propulsion. Math. Mech. Solids. 31, 1111–1125 (2026)
28. Eken, S., Kaya, M.O.: Flexural-torsional coupled vibration of anisotropic thin-walled beams with biconvex cross-section. Thin-Walled Struct. 94, 372–383 (2015)
29. Li, H.-C., Ke, L.-L., Yang, J., Kitipornchai, S., Wang, Y.-S.: Free vibration of variable thickness FGM beam submerged in fluid. Compos. Struct. 233, 111582 (2020)
30. Mahdavi, M.H., Farshidianfar, A., Tahani, M., Mahdavi, S., Dalir, H.: A more comprehensive modeling of atomic force microscope cantilever. Ultramicroscopy 109, 54–60 (2008)
31. Ruge, P., Birk, C.: A comparison of infinite Timoshenko and Euler–Bernoulli beam models on Winkler foundation in the frequency- and time-domain. J. Sound. Vib. 304, 932–947 (2007)
32. Stempin, P., Sumelka, W.: Dynamics of Space-Fractional Euler–Bernoulli and Timoshenko Beams. Materials 14, 1817 (2021)
33. Timoshenko, S.P.: LXVI. On the correction for shear of the differential equation for transverse vibrations of prismatic bars. Philos. Mag. J. Sci. 41, 744–746 (1921)
34. Huang, T.C.: The Effect of Rotatory Inertia and of Shear Deformation on the Frequency and Normal Mode Equations of Uniform Beams With Simple End Conditions. J. App. Mech. 28, 579–584 (1961)
35. Morison, J.R., Johnson, J.W., Schaaf, S.A.: The Force Exerted by Surface Waves on Piles. J. Pet. Technol. 2, 149–154 (1950)
36. Morison, J.R., Johnson, J.W., O'Brien, M.P.: Experimental studies of forces on piles. Coast. Eng. Proc. 1, 25 (1953)
37. Takada, Y., Nakanishi, Y., Araki, R., Nonogaki, M., Wakisaka, T.: Effect of Material and Thickness about Tail Fins on Propulsive Performance of a Small Fish Robot. J. Aero Aqua Bio-mech. 1, 51–56 (2010)

38. Shabana, A.A.: Dynamics of Multibody Systems, 4 ed. Cambridge University Press, Cambridge (2013)
39. Lighthill, M.J.: Large-amplitude elongated-body theory of fish locomotion. Proc. R. Soc. B: Biol. Sci. 179, 125–138 (1971)
40. Païdoussis, M.P., Price, S.J., De Langre, E.: Fluid-structure interactions. Cambridge University Press (2010)
41. Cowper, G.R.: The Shear Coefficient in Timoshenko's Beam Theory. J. App. Mech. 33, 335–340 (1966)